RSC Advances

ROYAL SOCIETY OF CHEMISTRY

PAPER

View Article Online
View Journal | View Issue

Cite this: *RSC Adv.*, 2026, **16**, 12458

A spatiotemporally controlled MNE@PDA-Diz/GP hydrogel system: enhancing spinal cord injury repair *via* ROS scavenging, calcium influx inhibition, and macrophage polarization

Xin Bao,†[a] Jingyan Sun,†[b] Xing Gao,†[a] Mingsheng Xu,[c] Chen Dong*[d] and Honghua Pan *[a]

Spinal cord injury (SCI) is a severe type of central nervous system trauma. It not only causes the loss of sensory and motor function but also triggers a series of secondary injuries, especially oxidative stress and inflammation. Current therapeutic methods fail to effectively address the multi-pathological cascade reactions, highlighting an urgent need for integrated treatment strategies that can simultaneously repair the damaged microenvironment and promote neural regeneration. In this study, a multifunctional thermosensitive MNE@PDA-Diz/GP hydrogel was designed. We incorporated a core–shell structured manganese nanozyme@polydopamine (MNE@PDA), modified with dizocilpine, into gelatin methacryloyl and a poly(*N*-isopropylacrylamide) hydrogel (GP hydrogel), featuring a thermosensitive polymer. The MNE@PDA-Diz/GP hydrogel, which was crosslinked under UV-vis light, provides a biocompatible three-dimensional scaffold that mimics the natural mechanical properties of the spinal cord, thereby supporting cell adhesion and proliferation. Meanwhile, the photothermal properties of polydopamine and the thermosensitivity of poly(*N*-isopropylacrylamide) enable spatiotemporally controlled release of dizocilpine. These three components work in synergy: the manganese nanozyme scavenges reactive oxygen species to exert anti-oxidative effects, polydopamine modulates macrophage polarization to alleviate inflammation, and dizocilpine inhibits calcium influx to provide neuroprotection. This work presents a novel and versatile platform for multi-targeted SCI therapy and promotes the development of regenerative strategies.

Received 18th November 2025
Accepted 16th February 2026

DOI: 10.1039/d5ra08918b

rsc.li/rsc-advances

Introduction

Spinal cord injury (SCI) is a severe type of central nervous system trauma that disrupts communication between the brain and the body, leading to permanent sensory-motor deficits. The initial mechanical damage is compounded by a cascade of secondary injuries, including ischemia, excitotoxicity, oxidative stress, and neuroinflammation, which collectively exacerbate neural loss and hinder recovery.[1] Furthermore, glial scar formation creates a persistent physical and chemical barrier to regeneration.[2] As reported by the National Spinal Cord Injury Statistical Center in 2021, around 296 000 individuals in the United States are living with SCI, with an estimated annual increase of 17 900 cases.[3] Despite the accumulation of extensive research findings on SCI treatment, existing therapeutic approaches face significant constraints. Current clinical management of SCI primarily relies on surgical decompression to relieve mechanical compression, short-term administration of corticosteroids such as methylprednisolone to mitigate acute inflammation, and long-term rehabilitation training to compensate for functional deficits.[4] However, these strategies suffer from notable limitations. Surgical intervention only halts the progression of primary injury but fails to modulate the cascading pathological reactions of secondary injury, such as inflammatory storms, oxidative stress, and glial scar formation. Systemic drug delivery often leads to severe off-target side effects and low bioavailability at the injury site, as therapeutic agents struggle to penetrate the blood-spinal cord barrier. Rehabilitation training merely achieves partial functional compensation without addressing the root causes of neural regeneration failure.[5] Moreover, these conventional methods are inadequate in overcoming age-related barriers, such as declined proliferation and differentiation potential of neural stem cells and exacerbated inhibitory microenvironment in aging individuals, resulting in suboptimal repair outcomes. Hence, there is an urgent necessity to work out integrated

---

[a] *Yixing People's Hospital, China. E-mail: staff1108@yxph.com*
[b] *Nanjing Foreign Language School, China*
[c] *Suzhou Institute of Nano-tech and Nano-Bionics Chinese Academy of Sciences, China*
[d] *Ningbo University of Finance & Economics, China. E-mail: dongchen@nbufe.edu.cn*

† These authors contributed equally to this work.

therapeutic approaches that can repair the damaged microenvironment and promote nerve regeneration simultaneously.

The pathophysiology of SCI presents several interconnected therapeutic targets. Excitotoxicity, driven by excessive glutamate release and overactivation of *N*-methyl-D-aspartate receptors (NMDARs), leads to cytotoxic calcium influx and neuronal death.[6] While NMDAR antagonists like dizocilpine (Diz) can block this pathway,[7] their systemic use is limited by off-target effects and a narrow therapeutic window,[8] underscoring the need for localized, controlled delivery. Meanwhile, highly activated neural cells caused by calcium overload will accelerate mitochondrial dysfunction and excessive reactive oxygen species (ROS) release.[9] Excessive ROS promotes inflammatory cascade reactions, which aggravate scar formation. The surface-active sites of nanozymes can mimic natural antioxidant enzymes by undergoing redox reactions with ROS. A representative example is the PCN-224 (Mn) MOF nanozyme, which features a Mn–N_4 structure that confers catalase-like activity. It efficiently converts accumulated hydrogen peroxide at injury sites into water and oxygen, alleviating oxidative stress and supplementing local oxygen levels.[10] However, their potential cytotoxicity and lack of targeting remain concerns.[11]

Another complication arises from the formation of scar tissue at the injury site, which acts as a physical barrier, impeding nerve fiber growth and neural regeneration.[12] This fibrotic scar primarily stems from inflammatory responses following injuries: activated astrocytes proliferate and undergo reactive gliosis, forming a dense glial scar.[4] To address this, polydopamine (PDA), a natural biomimetic polymer inspired by mussel adhesion proteins, has emerged as a promising multifunctional material.[13] Dopamine spontaneously polymerizes under weak alkaline conditions to form adherent, biocompatible films. The core functionality of PDA originates from its catechol and amine groups, which confer potent anti-inflammatory and antioxidant properties. These groups enable PDA to scavenge free radicals, chelate metal ions, and regulate inflammatory factors, thereby alleviating oxidative stress and inflammation.[14] In neural regeneration, PDA acts through multiple mechanisms: it can release neurotrophic factors, regulate intracellular signaling, and foster a pro-regenerative microenvironment for axon growth.[15] This is exemplified by studies showing PDA-modified chitin conduits not only sustainably release therapeutic exosomes but also directly stimulate Schwann cells to enhance secretion of key neurotrophic factors (nerve growth factor, brain-derived neurotrophic factor, and ciliary neurotrophic factor).[16] Consequently, *in vivo* implantation of such PDA-based constructs can improve the inhibitory SCI microenvironment by scavenging

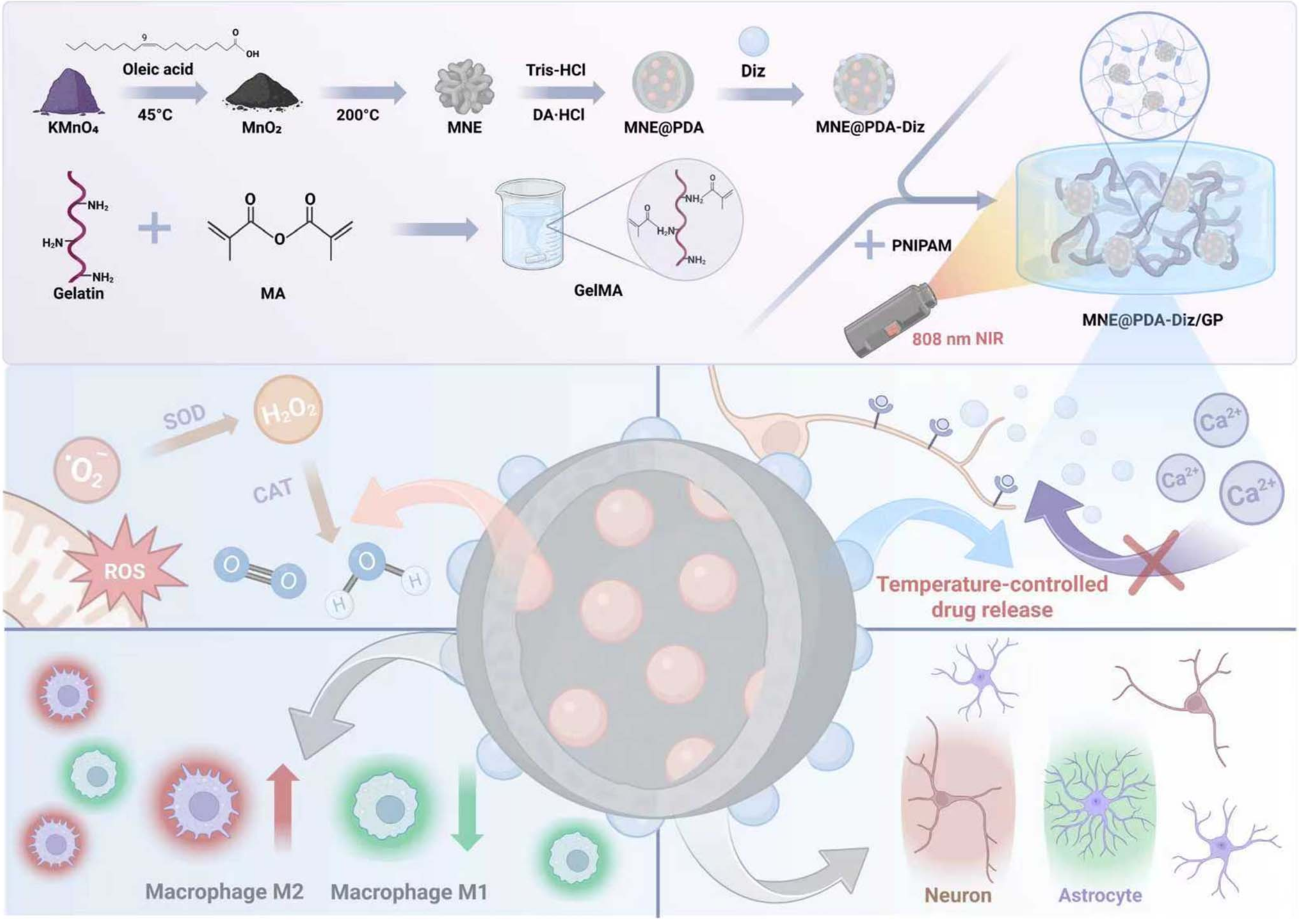

Scheme 1

ROS, suppressing glial scar formation, and modulating microglial polarization furthermore, the strong near-infrared (NIR) absorptioncapacity of PDA, enables photothermal therapy (PTT).[13] This property allows for NIR-triggered, spatiotemporally precise drug release, adding a layer of controllable therapeutic intervention to its repertoire.

To integrate these therapeutic actions, an advanced delivery platform is essential. Hydrogels, with their tunable physical properties, tissue-like water content and excellent biocompatibility, have emerged as ideal scaffolds for neural repair. These properties enable them to provide mechanical support for cell growth, facilitate nutrient and metabolite exchange, and serve as carriers for controlled drug delivery or cell transplantation. In neural regeneration, hydrogels can create a protective microenvironment to reduce inflammation, guide axonal extension, and promote tissue integration.[17] Nevertheless, single-component hydrogels often come with limitations. For instance, natural hydrogels may lack sufficient mechanical strength or have degradation rates that are difficult to control, while synthetic hydrogels may suffer from poor cell adhesion or low biological activity.[18] Gelatin methacryloyl (GelMA), a photo-crosslinkable natural polymer derived from gelatin, combines the biocompatibility of natural ECM with tunable mechanical properties, making it capable of supporting cell adhesion, proliferation and differentiation through its RGD peptide sequences.[19] Poly(*N*-isopropylacrylamide) (PNIPAM), a well-studied thermosensitive synthetic polymer, undergoes a reversible phase transition near physiological temperature (≈32 °C). Above this temperature, PNIPAM chains transition from a hydrophilic to a hydrophobic state, causing the hydrogel network to shrink. This temperature-responsive behavior enables on-demand regulation of drug release and scaffold degradation.[20] By combining GelMA and PNIPAM, the resulting GelMA-PNIPAM (GP) composite hydrogel integrates the biological activity of GelMA with the thermosensitive functionality of PNIPAM, overcoming the limitations of single-component systems and providing a versatile platform for spatiotemporally controlled neural regeneration therapy.

In this work, we designed a multifunctional thermosensitive hydrogel system (MNE@PDA-Diz/GP) for synergistic SCI repair (Scheme 1). The core of our strategy is to prepare a core–shell nanoparticle, where the manganese nanozyme (MNE) is coated with a polydopamine (PDA) layer and loaded with dizocilpine (Diz). This construct is then embedded within a GP hydrogel. The system is engineered to perform four key functions: (1) the MNE core scavenges excessive intracellular ROS and Ca^{2+} influx to alleviate oxidative stress; (2) the released Diz released Diz inhibits NMDAR-mediated excitotoxicity; (3) the PDA shell modulates macrophage polarization towards an anti-inflammatory M2 phenotype, further mitigated by PTT; and (4) the thermosensitive GP hydrogel provides a biocompatible, permissive scaffold for neural cells while enabling NIR-triggered, spatiotemporally controlled drug release. We comprehensively characterize the physicochemical properties of this composite system and demonstrate its efficacy *in vitro* in regulating ROS scavenging, macrophage polarization, and NSC migration. This integrated approach offers a novel and potent strategy for addressing the complex pathophysiology of SCI through coordinated multi-target intervention.

Experimental

Materials

Potassium permanganate, anhydrous ethanol, Tris-HCl buffer solution, and NaOH solution were obtained from Sinopharm Group Co., Ltd, China. Oleic acid and dizocilpine hydrogen maleate were purchased from Aladdin Biochemical Technology Co., Ltd, Shanghai, China. Dopamine hydrochloride, anhydrous DMSO, gelatin, methacrylate (MA), and 2′,7′-dichlorodihydrofluorescein diacetate (DCFH-DA probe) were obtained from Sigma-Aldrich, St. Louis, MO, USA. Phosphate-buffered saline (PBS) was obtained from Meilun Biotechnology Co., Ltd, Dalian, China. HT22 cell lines were purchased from Tansoole Co., Ltd, Shanghai, China.

Preparation of MNE and MNE@PDA-Diz

First, 1.0 g of potassium permanganate was weighed using an electronic analytical balance (ML204L, METTLER TOLEDO, Switzerland) and dissolved in 500 mL of deionized water prepared using a water purification system (Milli-Q Reference A+, Merck, Germany). The dissolution was carried out with magnetic stirring for 30 minutes. Subsequently, 10 mL oleic acid was added dropwise into the reaction mixture, followed by a 28 °C water bath (Bilon HH-4, Shanghai, China) and a continuous swirling for 24 hours. The black suspension obtained was then centrifuged at 12 000 rpm for 20 minutes with a centrifuge (Eppendof Centrifuge 5452R, Germany) to separate the precipitate. The solid collected was then washed three times in turn with ionized water and anhydrous ethanol, followed by vacuum drying at 45 °C overnight to yield MnO_2 nanoparticles. The as-synthesized MnO_2 was calcined in a muffle furnace (King Hong, China) at 200 °C to obtain monodisperse MNE.

For surface modification, 40 mg MNE was dispersed in 80 mL ethanol and mixed with a 120 mg Tris-HCl solution containing dopamine hydrochloride (1.6 mg mL^{-1}). The reaction pH was adjusted to 7–8 and the mixture was stirred at room temperature for 24 hours, resulting in a black solution. The product was purified by repeated centrifugation and washing with deionized water and ethanol, followed by drying at 45 °C to afford the final PDA-coated MNE as a black powder.

The MNE were then coated with PDA through oxidative self-polymerization in Tris-HCl buffer with continuous oxygenation. For hydrophilization, the dizocilpine solution was diluted in a 10% organic solvent aqueous solution before use. The resulting PDA-coated nanozymes were subsequently incubated with the hydrophilized dizocilpine solution to facilitate drug adhesion. Dizocilpine solution was prepared by dissolving 1 mg of dizocilpine in 1 mL of 10% DMSO aqueous solution. Subsequently, 1 mg of MNE@PDA was added to the above solution, followed by continuous stirring at 4 °C for 24 hours to facilitate drug adhesion.The solution was centrifuged (12 000 × *g*, 15 minutes), filtered, and the supernatant liquid concentration was confirmed *via* high-performance liquid chromatograph (HPLC).

Preparation of GelMA

GelMA was synthesized as described previously.[19] Briefly, gelatin was dissolved in 50 mL deionized water at 50 °C to make a 10 wt% uniform solution. 1.6 mL methacrylate was added to the gelatin solution at a rate of 0.5 mL min^{-1} under stirring conditions, while the pH was maintaining at 7–8 with 1 M NaOH. The mixture was allowed to react at room temperature for 24 hours. The GelMA solution was dialyzed against deionized water using a 3500 Da cutoff dialysis tube for 48 hours to remove unreacted MA and other impurities. The GelMA solution was frozen, lyophilized using lyophilizer (Christ ALPHAl-4/LD Plus, Germany) and stored at −80 °C for further use.

The drug loading content (DLC) was calculated using the following formula: DLC (%) = (Mass of loaded Diz/mass of MNE@PDA) × 100%. The mass of loaded Diz was determined by measuring the absorbance of the supernatant before and after loading against a standard calibration curve. For UV-vis quantification of Diz at 220 nm, all absorbance measurements were corrected by subtracting the baseline absorbance of a control solution containing an equivalent amount of MNE@PDA nanoparticles without drug, incubated and processed under identical conditions. A standard calibration curve was established using the same solvent system.

Preparation of MNE@PDA-Diz/GP

400 mg mL^{-1} MNE@PDA-Diz was mixed with 6 wt% GelMA, 2 wt% PNIPAM (Aladdin P767389, China), and 0.4 wt% LAP then irradiated with UV light for 3–5 minutes to form hydrogel.

Characterization of MNE@PDA-Diz and MNE@PDA-Diz/GL

Internal structures of MNE and MNE@PDA-Diz were observed by transmission electron microscope (TEM, HITACHI HT7700, Japan). MNE and MNE@PDA-Diz were dissolved, dipped on copper mesh and dried. Morphology was observed at 80 kV. Dynamic laser scattering spectrometer (DLS, Malvern Zetasizer Nano, USA) was used to measure zeta potential, hydrated diameter and polydispersity index of MNE and MNE@PDA-Diz nanoparticles. Fourier-transform infrared spectroscopy was performed to confirm Chemical bonds (FTIR, Thermo Fisher, USA). X-ray photoelectron spectroscopy analysis was conducted to analyze surface elemental composition (XPS, Thermo Fisher, USA).

The structure of the hydrogel was analyzed using an X-ray diffractometry (XRD, Bruker AXS D8 Advance, Germany) using Cu Kα radiation over the range of 10 to 85° at a scanning speed of 0.08% per min. The results were compared with standard cards. The inter-crystalline index was calculated according to Bragg's equation:

$$n\lambda = 2d\sin\theta$$

For testing photothermal conversion efficiency, PDA was irradiated with 808 nm NIR and the temperature of PDA was measured at different time intervals.

The MNE@PDA-Diz/GL was freeze-dried. To preserve their intrinsic cross-linked architecture, the samples were frozen with liquid nitrogen. The freeze-dried hydrogels were then attached to conductive adhesive tape. A conductive gold layer was sprayed at the voltage of 30 mV for 3 minutes, and the morphology was detected by scanning electron microscope (SEM, HITACHI S-4800, Japan).

The hydrogel was freeze-dried, and the dry weight (W_0) was recorded. After rehydration with PBS, the samples were weighed (W) at 1, 3, 6, 12 and 24 hours. The swelling behavior of hydrogel was determined by the equation:

$$\text{Swelling ratio}(\%) = \frac{W - W_0}{W_0} \times 100\%$$

The mechanical properties of hydrogels, including their elastic modulus (G') and viscous modulus (G''), were characterized using a rotational rheometer (Malvern Kinexus pro+, USA). The compressive mechanical properties of the hydrogels were tested using a universal testing machine (Instron, Canada). The compressive modulus was calculated from the slope of the initial linear region (0–15% strain) of the stress–strain curve. *In vitro* degradation was studied by incubating preweighed freeze-dried hydrogel samples in PBS at 37 °C. At predetermined time points, samples were removed, rinsed, lyophilized, and weighed. The mass remaining percentage was calculated as (W/W_0) × 100%.

Photothermal performance measurement

An 808 nm NIR laser was applied to assess the photothermal properties of the MNE@PDA-Diz/GP hydrogel. Specifically, a 1.5 mL Eppendorf tube was used to hold each sample, which was then exposed to the 808 nm NIR laser. The irradiation was conducted for a predetermined duration under a fixed power condition of 0.75 W cm^{-2}. Throughout the irradiation process, an infrared thermometer (FLIR E4, USA) was used to record the temperature changes of the samples.

The *in vitro* drug release study was conducted by immersing the hydrogels in release medium at 37 °C under sink conditions. For the+ PTT group, samples were exposed to periodic NIR irradiation (808 nm, 0.75 W cm^{-2}, 2 min every 12 h). At defined intervals, supernatant was withdrawn and replaced with fresh medium. The concentration of released dizocilpine was determined by UV-vis spectroscopy at 220 nm against the calibrated standard curve. Cumulative release was calculated and plotted over time. Experiments were performed in triplicate using independently prepared batches.

Cell culture

HT22 cells were cultured, and 1 × 10^6 cells were seeded on the poly-D-lysine (Gibco, USA) coated cell culture plate and cultured for 24 hours. After that, cells on the plate were transferred to five new plates. The MNE, MNE@PDA, MNE@PDA-Diz and MNE@PDA-Diz/GP were subsequently added to different new plates respectively and cultured for another 24 hours. The cell proliferation after treating with the hydrogels were evaluated by Ki67 antibody (ab15580, Abcam, USA) and visualized with a confocal laser microscope (Olympus FV3000, Japan).

To assess the biosafety of photothermal treatment, cells cultured with the hydrogels were subjected to NIR irradiation (808 nm, 0.75 W cm^{-2}, for 30 seconds) mimicking the PTT regimen. Cell viability was then evaluated using CCK-8 assay and live/dead staining (Calcein-AM/PI) according to the manufacturer's protocols.

Cytotoxicity assay

After being cultured on different substrates for 24 hours, the cells were used to investigate the cytotoxicity of these substrates *via* the Cell Counting Kit-8 (CCK-8, Bimake, USA). MNE, MNE@PDA, MNE@PDA-Diz and MNE@PDA-Diz/GP were prepared, then HT22 cells were co-cultured with MNE, MNE@PDA, MNE@PDA-Diz and MNE@PDA-Diz/GP in different wells for 24 hours. Subsequently, 10 mL of CCK-8 solution was added to each well, followed by culturing the cells at 37 °C for 2 hours. In the end, the absorbance of different samples at 450 nm was detected using a microplate reader (BioTek Cytation 3, USA).

Macrophage polarization analysis

To polarize the M0 subtype macrophages to the M1 inflammatory-subtype, M0 macrophages were cultured with 20 ng mL^{-1} interferon-γ (IFN-γ, Novoprotein, China) and 100 ng mL^{-1} lipopolysaccharide (LPS) for 48 hours. After that, IFN-γ and LPS were replaced with fresh medium containing different hydrogels. After incubation for 24 hours, the effects of hydrogels on M1 macrophages regulation were evaluated by flow cytometry (FCM, Beckman Coulter CytoFLEX S).

ROS evaluation

The oxidative stress of HT22 cells was simulated by the addition of hydrogen peroxide to the culture medium. The hydrogel was first added to the medium containing hydrogen peroxide, and cultured at 37 °C for 24 h to react with ROS. A 6-well cell culture plate was used for seeding 1 × 10^6 HT22 cells. After adhesion for 24 hours, the conditioned medium was added to the plate to culture for another 24 hours, then ROS levels in HT22 cells were tested by 2′,7′-dichlorodihydrofluorescein diacetate (DCFH-DA probe D, Sigma, USA). DCFH-DA is cleaved by cytosolic esterase to produce DCFH, which is oxidized by ROS to form 2′,7′-dichlorofluorescein showing green fluorescence under fluorescence microscope (Microshot, China).

Ca^{2+} influx analyse by immunofluorescence

The different hydrogels were added to the NSC culture medium containing 20 μM NMDA agonist (Selleck, S1060, USA), respectively. Then incubate NSCs with intracellular Ca^{2+} influx for 24 hours. NSCs incubated with different hydrogels were evaluated by 4 μM Fluo-4 AM probe (Beyotime, S1060, China) For 30 minutes at 37 °C in the dark and captured by a confocal laser microscope.

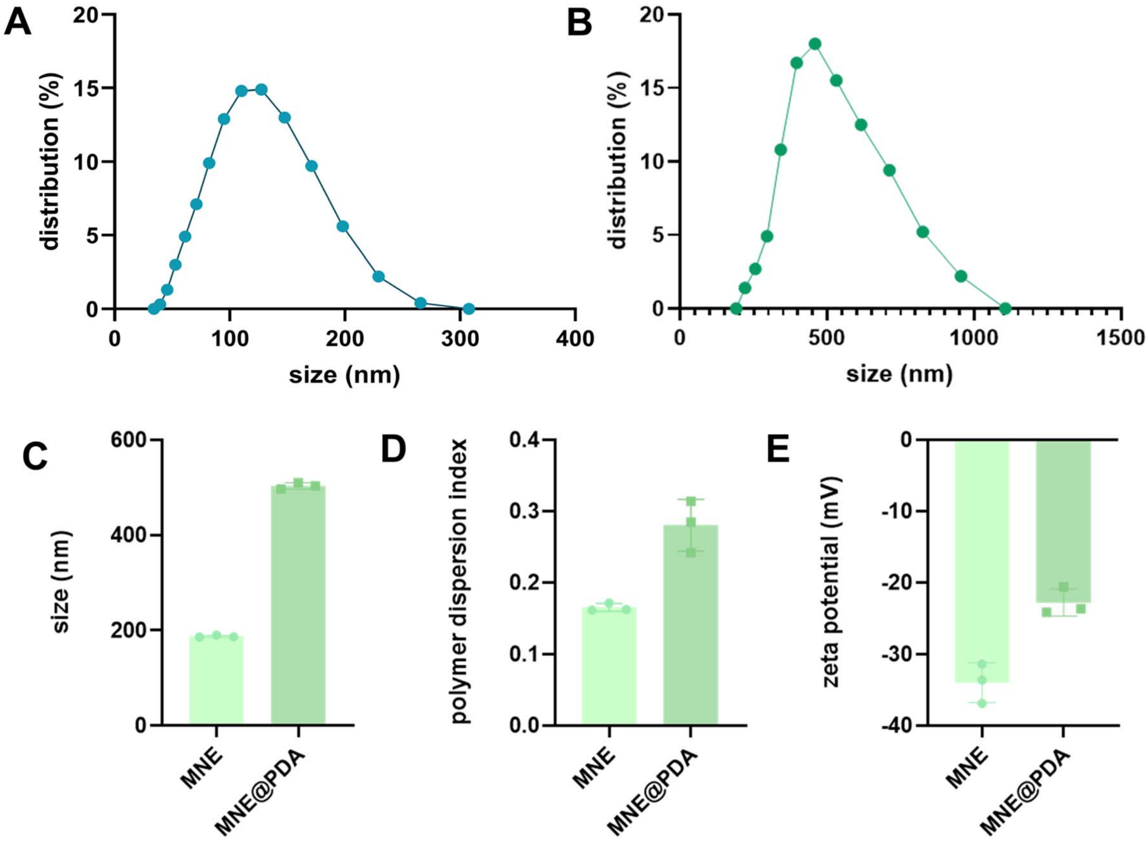

Fig. 1 The hydrated size and zeta potential of MNE and MNE@PDA by DLS. Hydrated size distribution of (A) MNE and (B) MNE@PDA. (C) Hydrated size of MNE and MNE@PDA. (D) PDI of MNE and MNE@PDA. (E) Zeta potential of MNE and MNE@PDA.

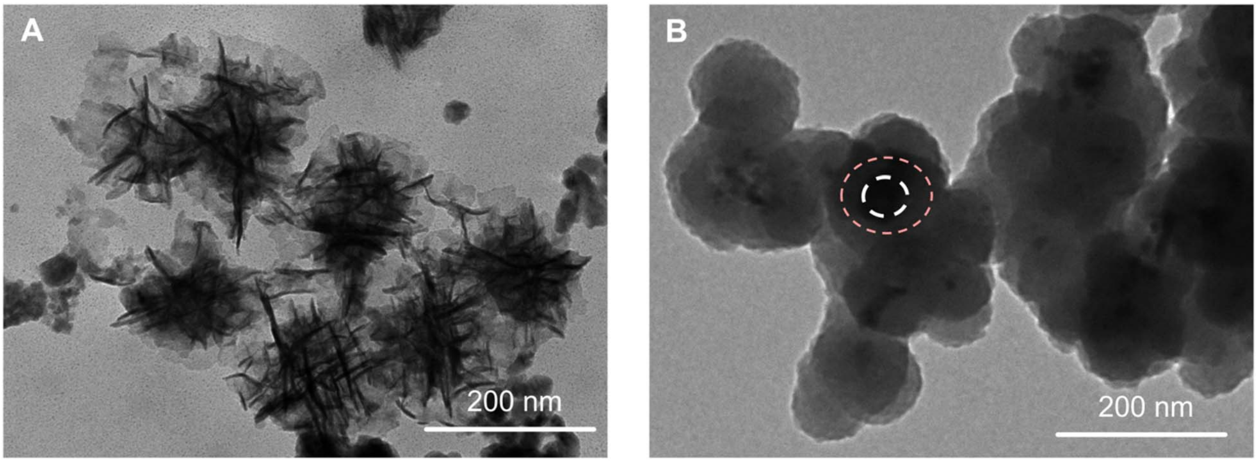

Fig. 2 TEM images of (A) MNE and (B) MNE@PDA.

Cell migration assay

Cells were digested with trypsin to prepare the cell suspension. The cell suspension was spread on a plate followed by cell counting with a cell counter (Countstar Biotech IC 1000, China). After that, the plate was placed in a cell incubator until the plate is completely covered by cells on the second day. A ruler was used as reference and a 10 μL syringe was used to create cell scratches. The plate was washed with PBS for three times to throughly remove the floating cells. After washing, the residual PBS in the plate was discarded, and serum-free medium was added to the plate. Before taking photos, the plate was washed 3 times using PBS to remove the floating cells. The widths of the scratch area in the photos were measured, and the migration distances of cells were calculated to evaluate the effects of materials on cell migration.

Cell proliferation and differentiation assay by RT-qPCR experiment

Approximately 1×10^7 cells were treated with TRIzol (Invitrogen, USA). The cDNA synthesis kit (Yeasen, 11123ES60, China) was used to perform reverse transcription, and RT-qPCR experiments were conducted using a SYBR GREEN dye kit (Yeasen, 11184ES08, China) and RT-qPCR instrument (Roche LightCycler 480II, Switzerland). The data obtained from the samples was normalized against glyceraldehyde 3-phosphate dehydrogenase (GAPDH) and analyzed using the delta/delta Ct method.

Statistics

All results are expressed as mean ± SD and statistically analyzed using an independent *T*-test for comparisons between two groups and one-way ANOVA for comparisons among multiple groups followed by Tukey's post hoc test. Specifically, *, ** and *** indicate $p < 0.05$, $p < 0.01$ and $p < 0.001$, respectively; and $p < 0.05$ was considered to indicate statistical significance.

Results

Synthesis and characterization of MNE@PDA-Diz

All biomaterials were prepared following the experimental section, as outlined in the procedure (1). Through self-polymerization of dopamine and oxidation of MnO_2, MNE@PDA was prepared. The size distribution of MNE and

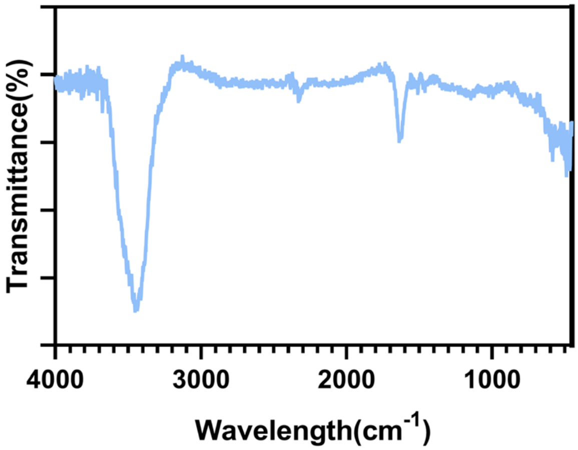

Fig. 3 Fourier-transform infrared (FTIR) spectra of MNE and MNE@PDA.

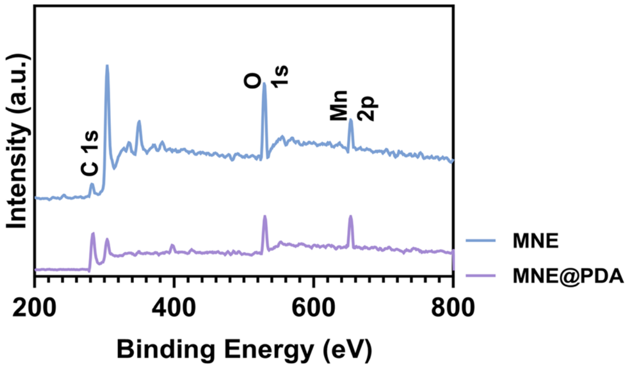

Fig. 4 X-ray photoelectron spectroscopy (XPS) survey spectra of MNE and MNE@PDA.

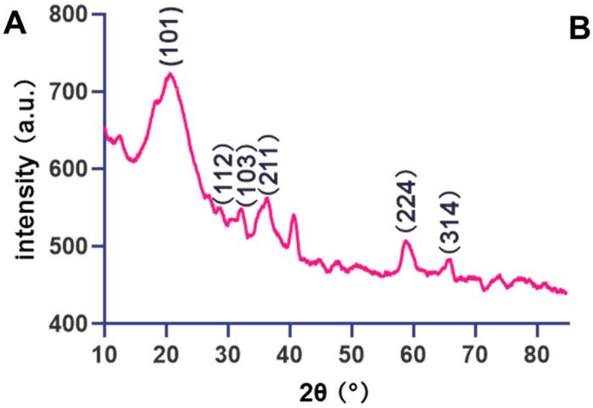

Fig. 5 XRD plots of intensity *vs.* 2-theta for (A) MNE and (B) MNE@PDA.

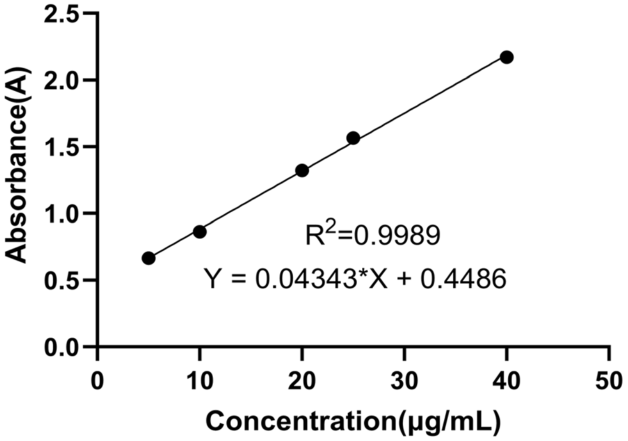

Fig. 6 Standard calibration curve for the quantification of dizocilpine. The curve was established by measuring the absorbance at 220 nm using UV-vis spectroscopy. Each data point represents the mean ± standard deviation ($n = 3$).

MNE@PDA was measured (Fig. 1A and B). The range of MNE was 29.4 to 356.2 nm, and the range of MNE@PDA was 190.1 to 1106.0 nm. The results both satisfied the normal distribution. Further comparison of the average hydrated sizes of the two materials (Fig. 1C) showed that the size changed from 187.7 ± 2.2 nm for MNE to 503.6 ± 6.8 nm for MNE@PDA, indicating that PDA effectively wrapped around MNE to form a core–shell structure with a shell thickness of approximately 315.9 nm. Further PDI data (Fig. 1D) showed that both biomaterials had good homogeneity with average values of 0.166 ± 0.006 and 0.280 ± 0.036, respectively. Zeta potential tests (Fig. 1E) showed that the potential of MNE was −34.0 ± 2.8 mV and that of MNE@PDA was −22.8 ± 1.9 mV. This change indicated that after PDA wrapping, the surface charge density of the material decreased, possibly because the shell structure altered the surface charge distribution. The broader hydrodynamic size distribution observed in MNE@PDA could be attributed to the inherent adhesiveness of PDA, which may lead to the formation of a limited fraction of dimers or oligomers during the coating process. Nevertheless, the PDI remained at an acceptable level (0.280 ± 0.036), indicating a moderately dispersed system. This interpretation is further supported by transmission electron microscopy (TEM, Fig. 2B), which demonstrates that the individual core–shell morphology remains evident, and no large, dense aggregates dominate the sample. Moreover, the preserved colloidal stability is evidenced by a sufficient zeta potential (−22.8 ± 1.9 mV). Importantly, this mild polydispersity did not impede the core functionalities of the

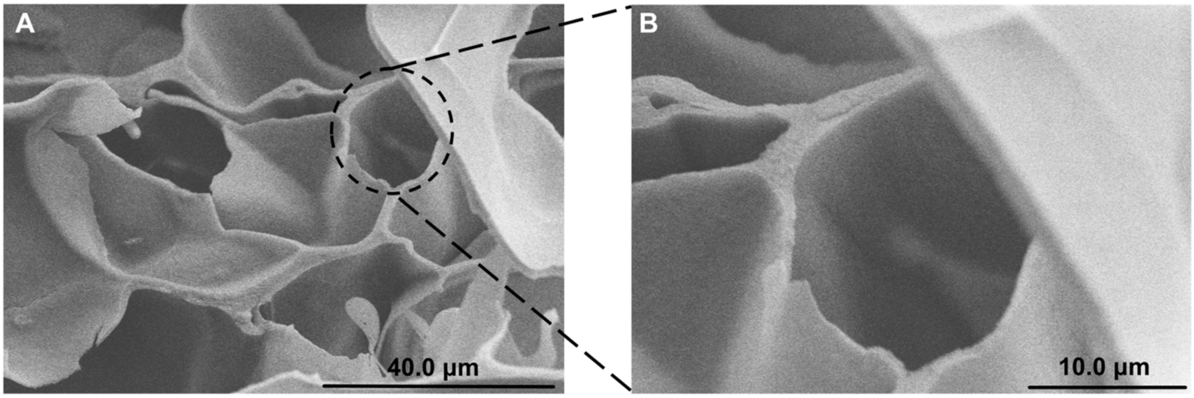

Fig. 7 The surface morphology of MNE@PDA-Diz/GP hydrogel at different scales. (A) MNE@PDA-Diz/GP at 40 μm; (B) MNE@PDA-Diz/GP at 10 μm.

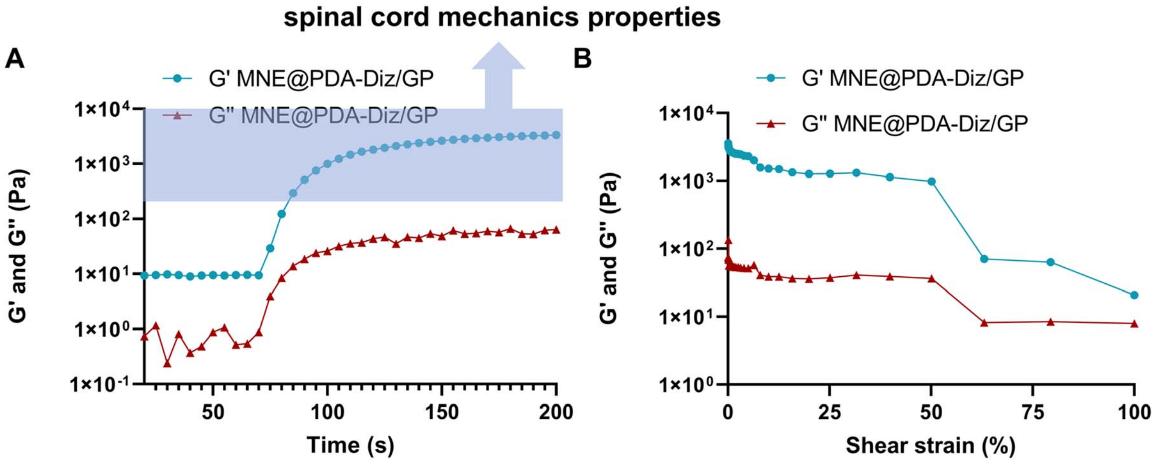

Fig. 8 The mechanical property of MNE@PDA-Diz/GP hydrogel. (A) Time-modulus curve and (B) strain-modulus curve are plotted using a rotational rheometer.

composite, such as drug loading and ROS scavenging, as demonstrated in subsequent experiments.

The internal structure of MNE and MNE@PDA was observed by TEM. In MNE, flower-like structure with high specific surface area was observed, which provides more active sites to bind with ROS (Fig. 2A). This provides better ROS scavenging ability for cell oxidative stress after SCI. Its surface was further coated with a layer of PDA. As a natural polymer secreted by mussels, a type of marine organisms, PDA has adhesiveness, NIR photothermal response properties, and certain anti-inflammatory effects. Through the self-polymerization reaction of dopamine, MNE was coated by PDA, enabling the nanoparticles to possess the properties of both MNE and PDA. Their core–shell structure is clearly shown in Fig. 2B.

To directly confirm the formation of the PDA coating on MNE, Fourier-transform infrared (FTIR) spectroscopy and X-ray photoelectron spectroscopy (XPS) analyses were performed. The FTIR spectrum of MNE@PDA (Fig. 3) exhibited a broad and strong absorption band around 3420 cm^{-1}, corresponding to the stretching vibrations of hydroxyl (–OH) and amine (–NH$_2$) groups in PDA. Additionally, a characteristic peak near 1602 cm^{-1}, attributed to the C═C stretching vibration of the benzene ring in PDA, was observed. The emergence of these characteristic IR peaks indicates the successful self-polymerization of dopamine and the formation of a PDA coating on the MNE surface, confirming the successful preparation of MNE@PDA nanoparticles.

Furthermore, XPS survey spectra of MNE and MNE@PDA (Fig. 4) provided direct evidence for the surface coating. The spectrum of MNE showed characteristic peaks for carbon (C 1s, ∼285 eV), oxygen (O 1 s, ∼532 eV), and manganese (Mn 2p, ∼640 eV). After PDA modification, the MNE@PDA spectrum showed a significant increase in the intensity of the C 1s peak, attributable to the carbon-rich PDA layer. Concurrently, the relative intensities of the O 1s and Mn 2p peaks decreased, as the PDA shell attenuated the photoelectron signals from the MNE core. These changes directly demonstrate the successful encapsulation of MNE by a PDA coating *via* oxidative self-polymerization.

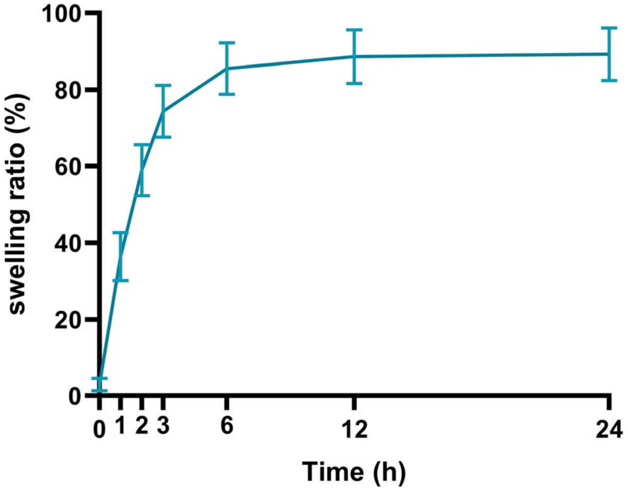

Fig. 9 The swelling performance of MNE@PDA-Diz/GP ($n = 3$).

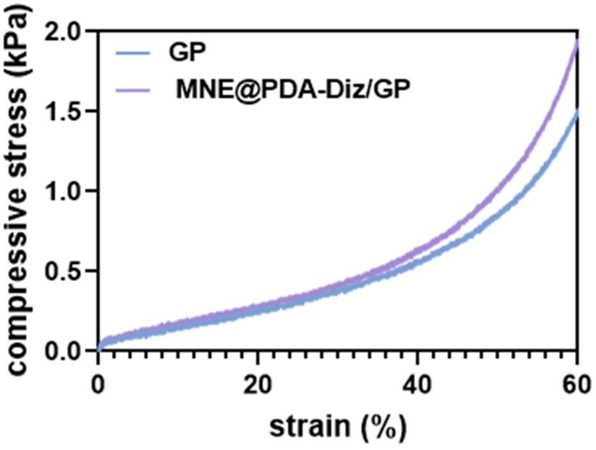

Fig. 10 Mechanical properties of the MNE@PDA-Diz/GP hydrogel.

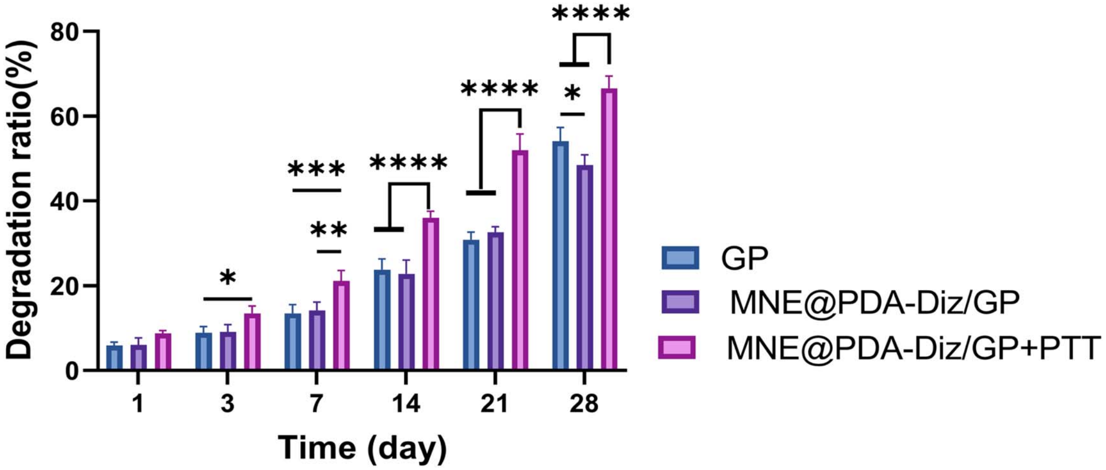

Fig. 11 *In vitro* degradation kinetics of the MNE@PDA-Diz/GP hydrogel.

Subsequently, the crystal structures of MNE and MNE@PDA were examined by X-ray diffraction (XRD). Six broad peaks of MNE were identified at 2θ angles of 20.7°, 26.8, 32.2°, 36.4°, 58.8°, and 66.0° (Fig. 5A). These peaks, which correspond to the (101), (112), (103), (211), (224), and (314) planes respectively (Mn, 04, JCPDS 80-0382), serve to confirm the XRD results. The crystal has the advantage of a slow degradation rate, thereby enhancing the stability of the material. The XRD pattern of MNE@PDA (Fig. 5B) displays a broad hump characteristic of amorphous materials, with no distinct diffraction peaks corresponding to crystalline MNE observable. This indicates that the diffraction signals from the crystalline MNE core are effectively shielded by the thick, uniform amorphous PDA coating. This result provides complementary evidence for the successful formation of a core–shell structure where the PDA shell is sufficiently thick to dominate the XRD profile.

The loading capacity and efficiency of dizocilpine onto the MNE@PDA were rigorously quantified. A standard calibration curve for dizocilpine was established using UV-vis spectroscopy at 220 nm, with appropriate baseline correction to account for potential background interference from PDA degradation products (Fig. 6). The drug loading content was determined by measuring the absorbance of the supernatant after the loading process and correlating it with the calibration curve. Results demonstrated that 1 mg of MNE@PDA nanoparticles could effectively load 116.3 ± 5.2 µg of Diz, confirming the successful and efficient drug incorporation into the core–shell system. This robust loading provides a solid foundation for the subsequent controlled release studies.

Characterization of MNE@PDA-Diz/GP hydrogel

Further, the nanoparticle MNE@PDA-Diz was mixed with GelMA and PNIPAM polymers to prepare the MNE@PDA-Diz/GP hydrogel. PNIPAM within this hydrogel exhibits temperature-sensitive properties. When the temperature exceeds 37 °C, the cross-linked network contracts, exposing isopropyl groups and transforming part of the hydrogel structure from hydrophilic to hydrophobic. The PTT property of PDA was leveraged to locally heat the hydrogel thus facilitating controlled drug release. The MNE@PDA-Diz/GP hydrogel features an interconnected, three-dimensional porous structure (Fig. 7), which serves as a carrier for nanoparticle delivery. Importantly, this nano/micro-porous architecture contributes significantly to water retention. The combination of capillary forces within the pores and the hydrophilic nature of the GelMA and PNIPAM polymer networks facilitates the immobilization of water molecules.

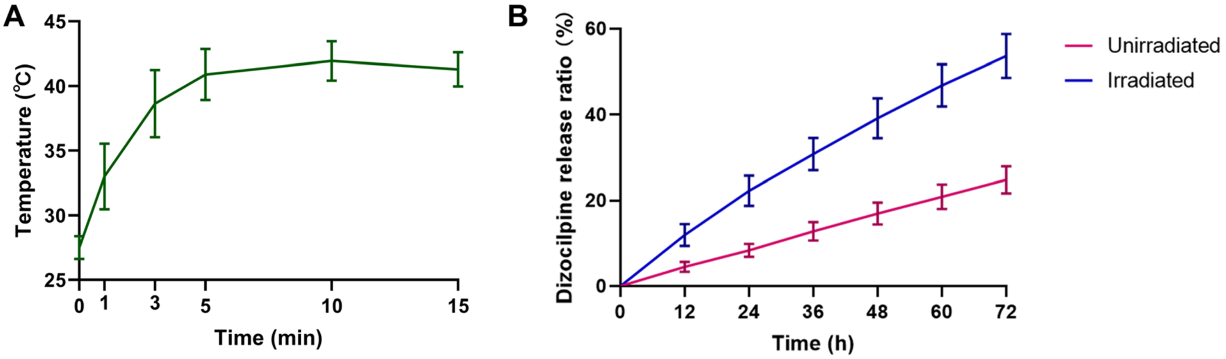

Fig. 12 The effects of the combined use of PTT and thermosensitive hydrogel MNE@PDA-Diz/GP. (A) PTT capability of MNE@PDA-Diz/GP under NIR irradiation ; (B) dizocilpine release ratio under irradiated and non-irradiated condition.

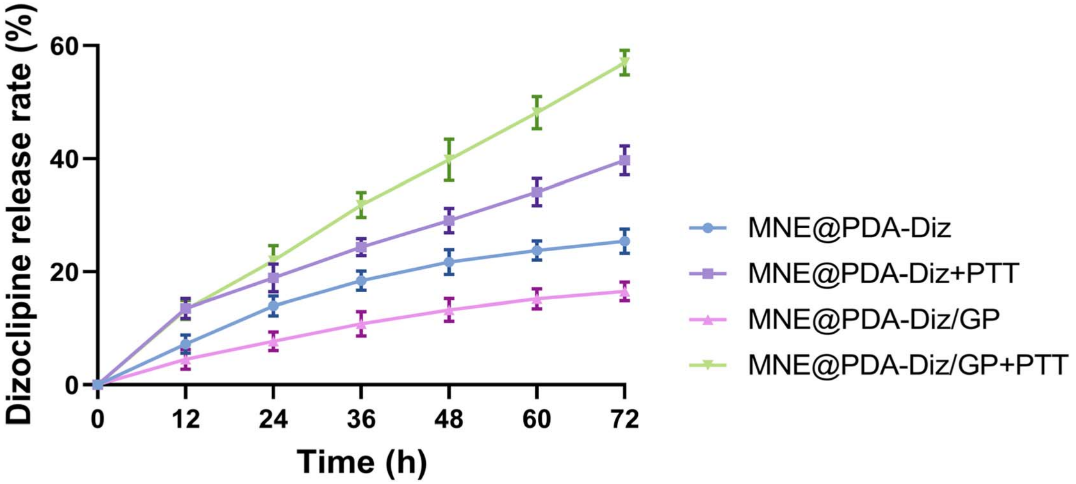

Fig. 13 Controlled release of dizocilpine from composite hydrogels under different conditions. Cumulative release profiles over 72 hours for four groups: MNE@PDA-Diz, MNE@PDA-Diz + PTT, MNE@PDA-Diz/GP, and MNE@PDA-Diz/GP + PTT. The MNE@PDA-Diz/GP + PTT group exhibited the most rapid and extensive release. Data are presented as mean ± SD ($n = 3$).

This mechanism helps to create and maintain a hydrated, tissue-like microenvironment at the injury site.

The elastic modulus and viscous modulus of the MNE@PDA-Diz/GP hydrogel were detected using a rotational rheometer. Fig. 8A showed the curing process of the hydrogel. A ultraviolet irradiation crosslinking was conducted on the hydrogel at 60 seconds. The results showed that the elastic modulus of the hydrogel underwent a jump starting from 70 seconds, which means the hydrogel began to transform from a liquid to an elastomer. After the completion of crosslinking, the elastic modulus reached 3185 Pa at 185 seconds. The elastic modulus of the hydrogel falls within the range that has been reported for native spinal cord tissue, which is typically on the order of ≤ 10 kPa.[21] This suggests a degree of mechanical compatibility with the host tissue environment, which can reduce rejection or inflammatory reactions during the transplantation process for spinal cord injury. In addition, this mechanical characteristic helps to support the proliferation and migration of nerve cells. Fig. 8B showed the ability of the material to store energy through elastic deformation. The high initial value indicates

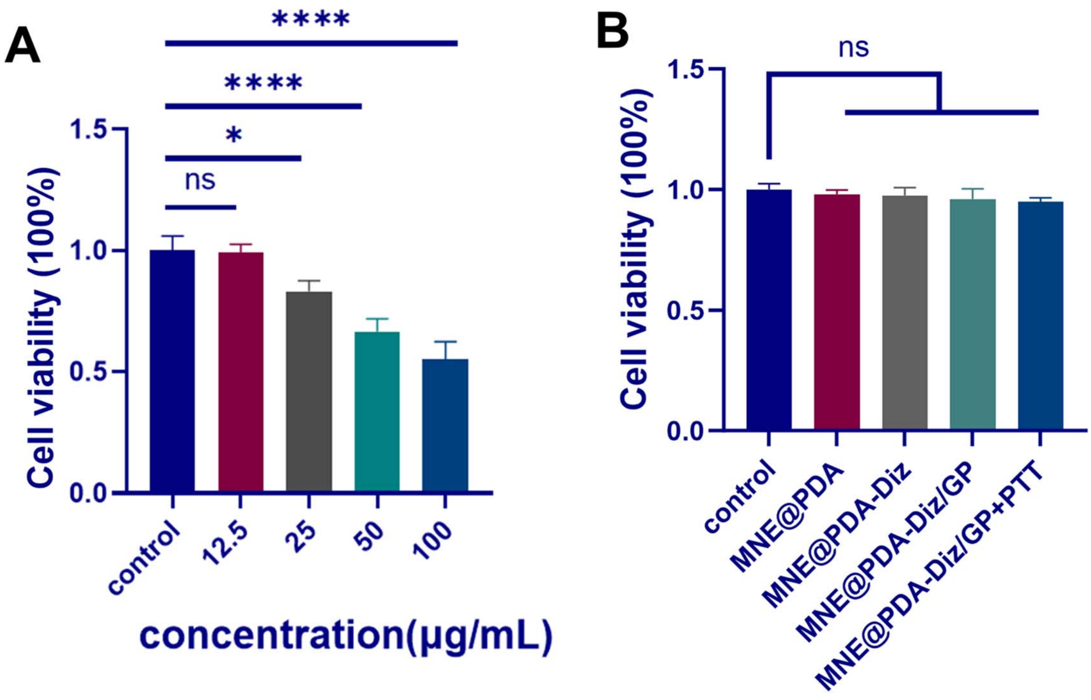

Fig. 14 The toxicity of MNE@PDA-Diz/GP hydrogel for NSCs. (A) The effects of different concentrations of MNE on viability of NSCs. (B) NSCs were treated with different groups of MNE, and CCK-8 assay was performed to measure cell viability.

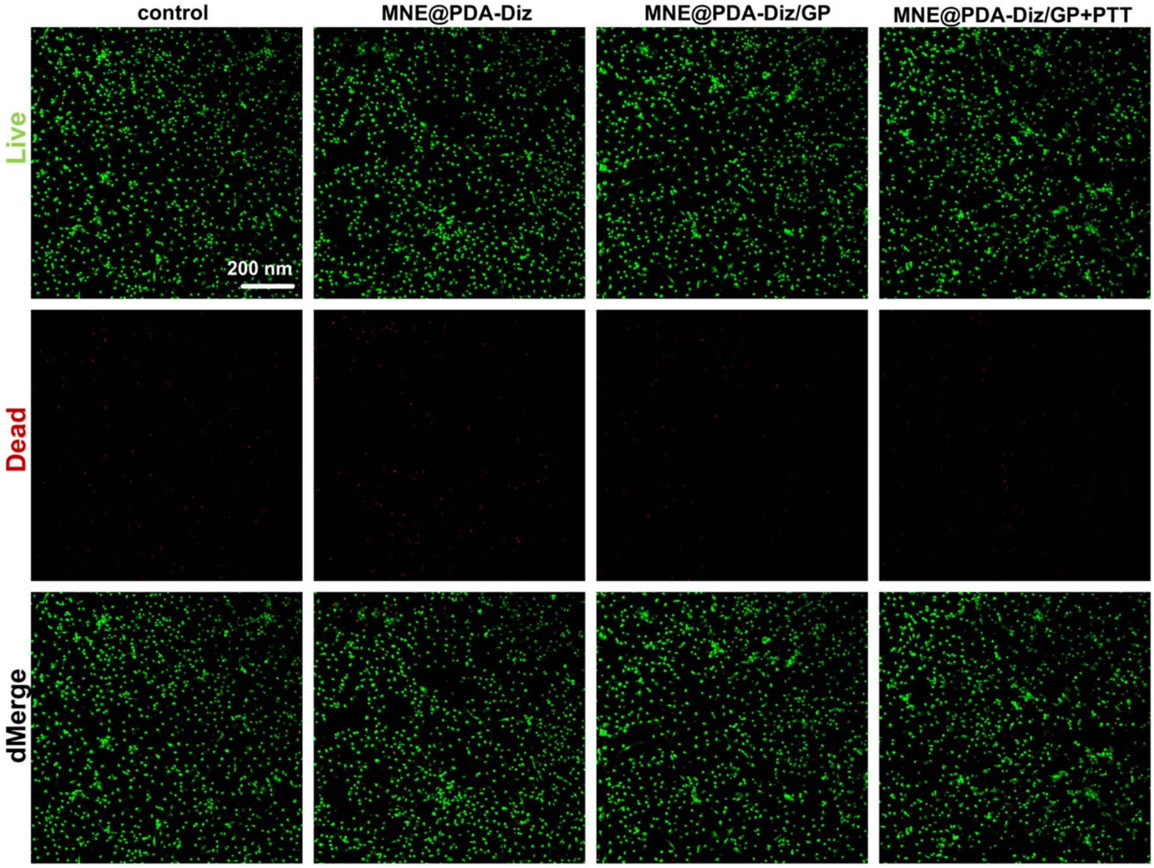

Fig. 15 Fluorescence microscopic images of live/dead staining assay of NSCs cultured with MNE@PDA-Diz, MNE@PDA-Diz/GP, and MNE@PDA-Diz/GP + PTT for 24 h.

that the initial elasticity of the material is good. As the shear strain increased, elastic moduludand viscous modulus decreased slowly in the early stage, and then decreased rapidly after the strain exceeded 50%, indicating that the elastic structure of the material was damaged by shearing and the deformation resistance is weakened.

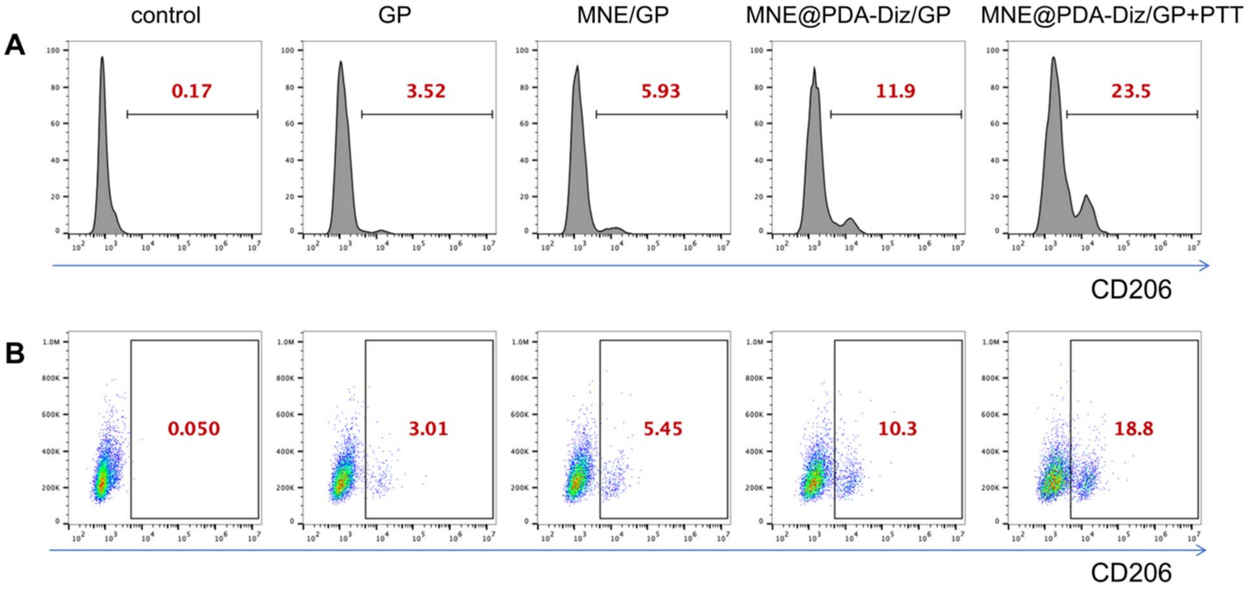

Fig. 16 The anti-inflammatory ability of MNE@PDA-Diz/GP + PTT. (A) Histograms of macrophage polarization induced by different materials and (B) Scatter plots of macrophage polarization induced by different materials detected by flow cytometry ($n = 3$).

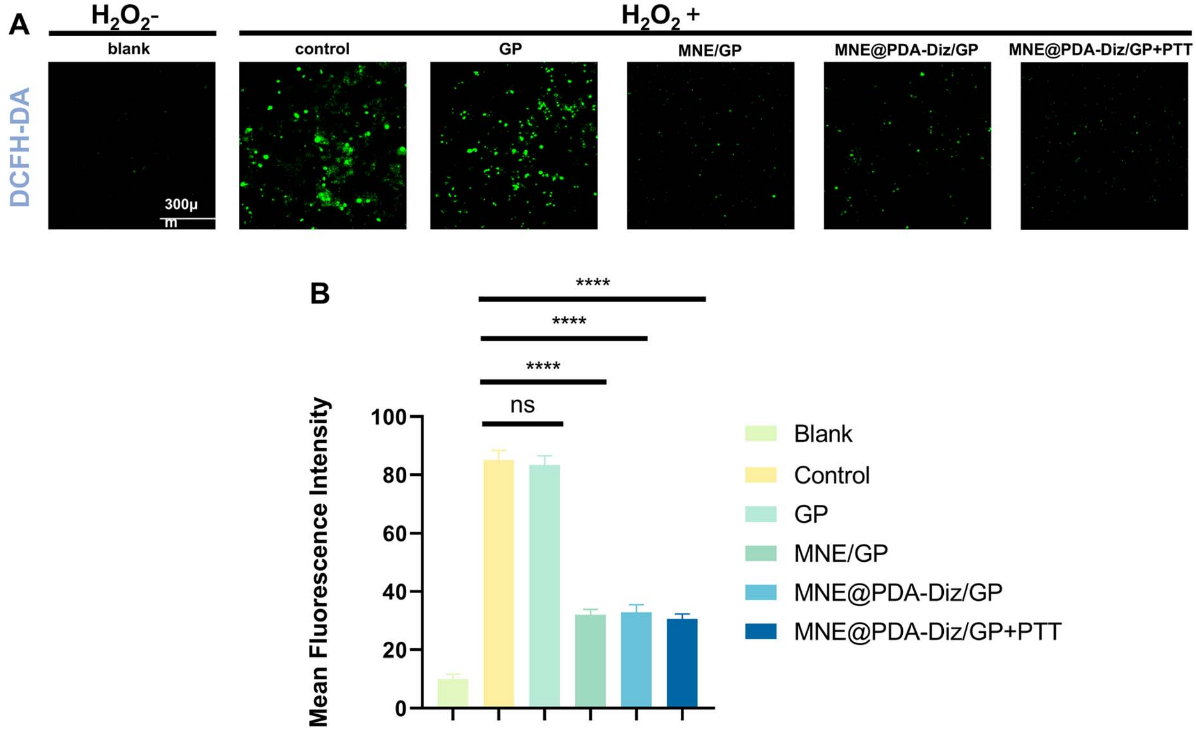

Fig. 17 ROS scavenging ability of MNE@PDA-Diz/GP + PTT. (A) H_2O_2-induced oxidative stress on HT22 cells treated by GP, MNE/GP, MNE@PDA-Diz/GP, MNE@PDA-Diz/GP + PTT are detected by confocal laser microscope. (B) the anti-oxidative effect of GP, MNE/GP, MNE@PDA-Diz/GP, and MNE@PDA-Diz/GP + PTT on the ROS levels induced by 0.2 mM H_2O_2.

The results showed that the hydrogel swelled rapidly from 0 to 3 hours; from 6 hours onwards, the swelling tended to stabilize, with the final swelling ratio reaching 89.2%. The occurrence of low swelling ratio is mainly related to GelMA and PNIPAM: GelMA is a material with high crosslinking density, characterized by a dense three-dimensional network structure that limits the penetration rate of water molecules; PNIPAM is a material with temperature-sensitive shrinkage regulation, characterized by volume shrinkage at physiological temperature (37 °C), which inhibits excessive water absorption. Hydrogel with a low swelling ratio can reduce compression on the surrounding spinal cord, resulting in small deformation and relatively slow degradation, and thus enabling long-term drug delivery (Fig. 9).

To evaluate the hydrogel's suitability as a scaffold for spinal cord tissue, its compressive mechanical properties were investigated under conditions simulating the physiological environment. Stress–strain curves (Fig. 10) revealed the typical nonlinear elastic behavior of a porous hydrogel.

The *in vitro* degradation profile of the MNE@PDA-Diz/GP hydrogel was monitored in PBS at 37 °C over a period of 28 days (Fig. 11). The hydrogel mass remaining decreased gradually over time, showing a sustained degradation profile suitable for long-term therapeutic support. By day 28, approximately 55% of the initial mass remained in PBS. This controlled degradation aligns with the desired timeframe for neural repair processes and ensures the scaffold maintains integrity during the critical early phase of healing.

Under NIR irradiation, the temperature of MNE@PDA-Diz/GP showed an increasing trend within 15 minutes, rising from 27.5 °C to 41.3 °C (Fig. 12A). Furthermore, based on the thermosensitive property of PNIPAM, the temperature elevation

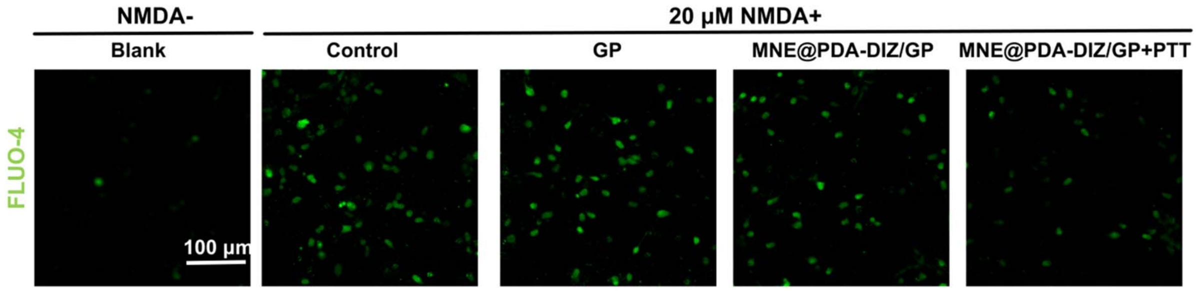

Fig. 18 The biological function of MNE@PDA-Diz/GP + PTT on regulation of NSCs and macrophages. Detection of intracellular calcium levels in NSCs was achieved *via* fluorescence imaging with the Fluo-4 AM probe used for staining ($n = 3$).

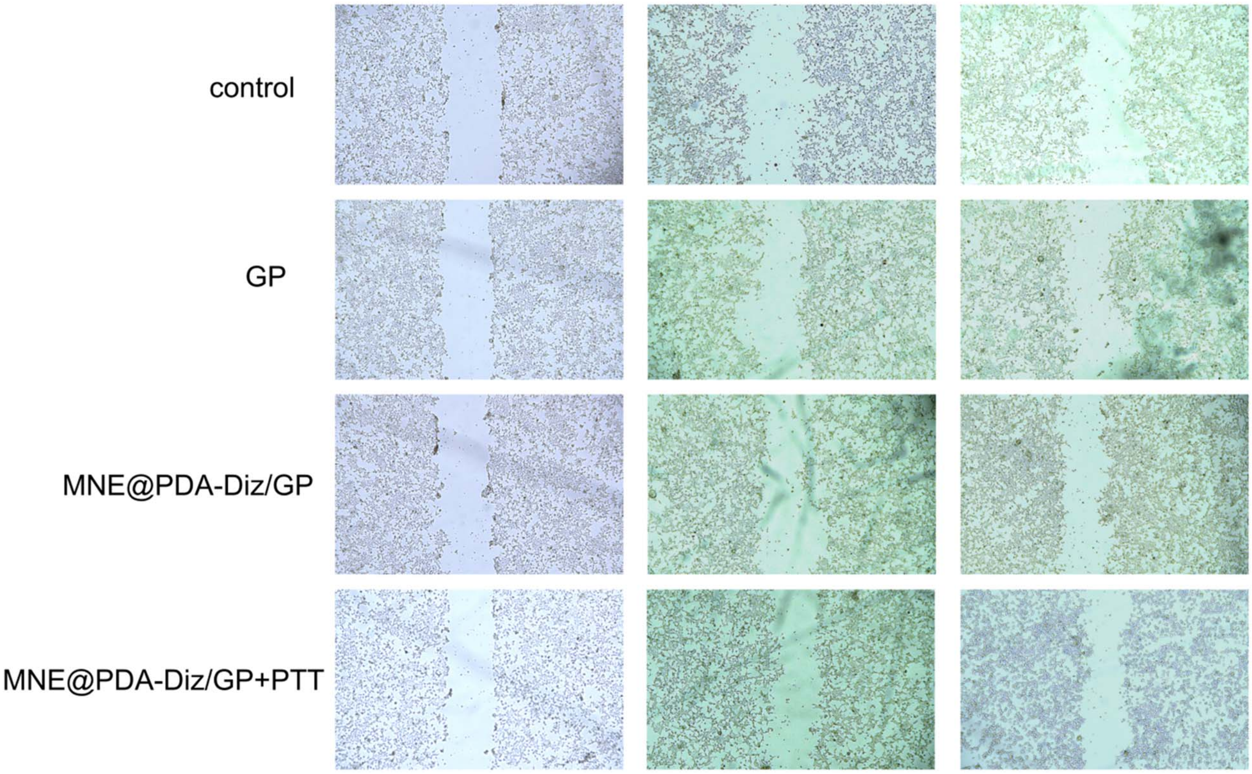

Fig. 19 MNE@PDA-Diz/GP + PTT promotes cell migration ability. Scratch experiment was performed with GP, MNE@PDA-Diz/GP, MNE@PDA-Diz/GP + PTT and the photos were taken by microscope ($n = 3$).

induced by PTT accelerated the release of dizocilpine. Fig. 12B showed that under irradiated and non-irradiated conditions, the gap in release ratio between two groups gradually widened over time. By 72 hours, the dizocilpine release ratio of the unirradiated group only reached 24.8 ± 3.2% while the irradiated group reached 53.7 ± 5.1%, presenting an overall trend of increasing difference.

The controlled release profiles of dizocilpine from the hydrogel under different conditions were systematically evaluated (Fig. 13). The cumulative release over 72 hours showed that the MNE@PDA-Diz/GP + PTT group achieved the most rapid and extensive release, significantly outperforming the groups without irradiation or without the PDA coating. This result directly demonstrates that the photothermal effect of PDA and the thermosensitivity of PNIPAM work in concert to enable on-demand, spatiotemporally controlled drug release.

Cell compatibility of MNE@PDA-Diz/GP hydrogel

The cytotoxic effects of the MNE nanozyme and MNE@PDA-Diz/GP hydrogel on NSCs were tested using CCK-8, a reagent that produces an absorance change through reactions with intracellular dehydrogenase. Firstly, different concentrations of MNE nanozyme were applied on NSCs to assess the toxic concentration. As shown in Fig. 14A, a concentration-dependent cytotoxicity was observed. A significant decrease in cell viability occurred when the MNE concentration exceeded 12.5 μg mL^{-1}. Therefore, the non-toxic concentration of 12.5 μg mL^{-1} was selected as the safe dose for the preparation of the hydrogel and for all subsequent experiments. As shown in Fig. 14B, the MNE@PDA-Diz/GP hydrogel formulated with this safe dose is is non-toxic.

Furthermore, to directly address the biosafety concern regarding the combined application of PTT and the hydrogel, we evaluated the cell viability under the actual therapeutic conditions. NSCs were cultured with the MNE@PDA-Diz/GP hydrogel and subjected to the same NIR irradiation protocol used for PTT (808 nm, 0.75 W cm^{-2}, for 30 s). Both CCK-8 assay and live/dead staining conducted after the treatment showed no significant cytotoxicity compared to the control groups without irradiation (Fig. 15).

Macrophage polarization reprogramming of MNE@PDA-Diz/GP hydrogel + PTT

Macrophages were first polarized to the pro-inflammatory M1 subtype using LPS and IFN-γ, and then treated with GP, MNE/GP, MNE@PDA-Diz/GP, and MNE@PDA-Diz/GP + PTT, respectively. The proportion of cells converted from M1 to M2 was then detected. CD206 is a marker of M2 macrophages. Fig. 16A showed that the fluorescence intensity of CD206-positive cells increased from 0.17% to 3.52%, 5.93%, 11.9%, and 23.5%, respectively. Further, Fig. 16B showed the ratios of CD206-positive cells increased from 0.05% to 3.01%, 5.45%, 10.3%, and 18.8%, respectively. All groups showed an increasing trend in the proportion of M2 cells, with relatively small increases in the first three groups. This moderate increase is due to MNE exerting antioxidant effects, which are associated with inflammatory responses modulation.[22] Notably, the strong anti-inflammatory activity of PDA is an important factor promoting the conversion of macrophages from M1 to M2. In addition, PTT can accelerate the release of loaded components, enabling faster onset of anti-inflammatory regulation. Notably, the MNE@PDA-Diz/GP and MNE@PDA-Diz/GP + PTT groups exhibited stronger anti-inflammatory ability.

ROS scavenging ability of MNE@PDA-Diz/GP hydrogel + PTT

The DCFH-DA probe was used to detect the level of H_2O_2-induced cellular oxidative stress under different materials and conducted quantitative analysis (Fig. 17A and B). As demonstrated by the results, the fluorescence intensity of the control group and the GP group was consistent. This indicates that GP does not possess ROS scavenging ability and is therefore unable to provide neuronal cells with effective antioxidant protection. The fluorescence intensity of the MNE/GP, MNE@PDA-Diz/GP, and MNE@PDA-Diz/GP + PTT groups was significantly reduced, with statistical significance, suggesting that MNE/GP, MNE@PDA-Diz/GP, and MNE@PDA-Diz/GP + PTT have ROS scavenging capabilities. This is because MNE can achieve the effect of scavenging ROS through changes in electron valence states.[23] Although the addition of PTT showed good effects in the drug release experiment, it did not produce a significant difference in the ROS experiment. This may be because the ROS inherently present in the cells was already close to equilibrium.

Ca^{2+} influx inhibition of MNE@PDA-Diz/GP hydrogel + PTT

The FLUO-4 calcium staining results clearly demonstrated the neuroprotective efficacy of the MNE@PDA-Diz/GP hydrogel against NMDA-induced excitotoxicity (Fig. 18). The blank group showed minimal FLUO-4 fluorescence, indicating normal calcium homeostasis. However, exposure to 20 μM NMDA led to intense fluorescence in the control group, reflecting severe calcium overload. In contrast, the MNE@PDA-Diz/GP hydrogel significantly reduced calcium influx, as evidenced by diminished fluorescence. Notably, the combination with PTT further enhanced this effect, yielding the lowest fluorescence intensity. This confirms that the hydrogel integrates multiple therapeutic mechanisms including dizocilpine inhibits NMDA receptor

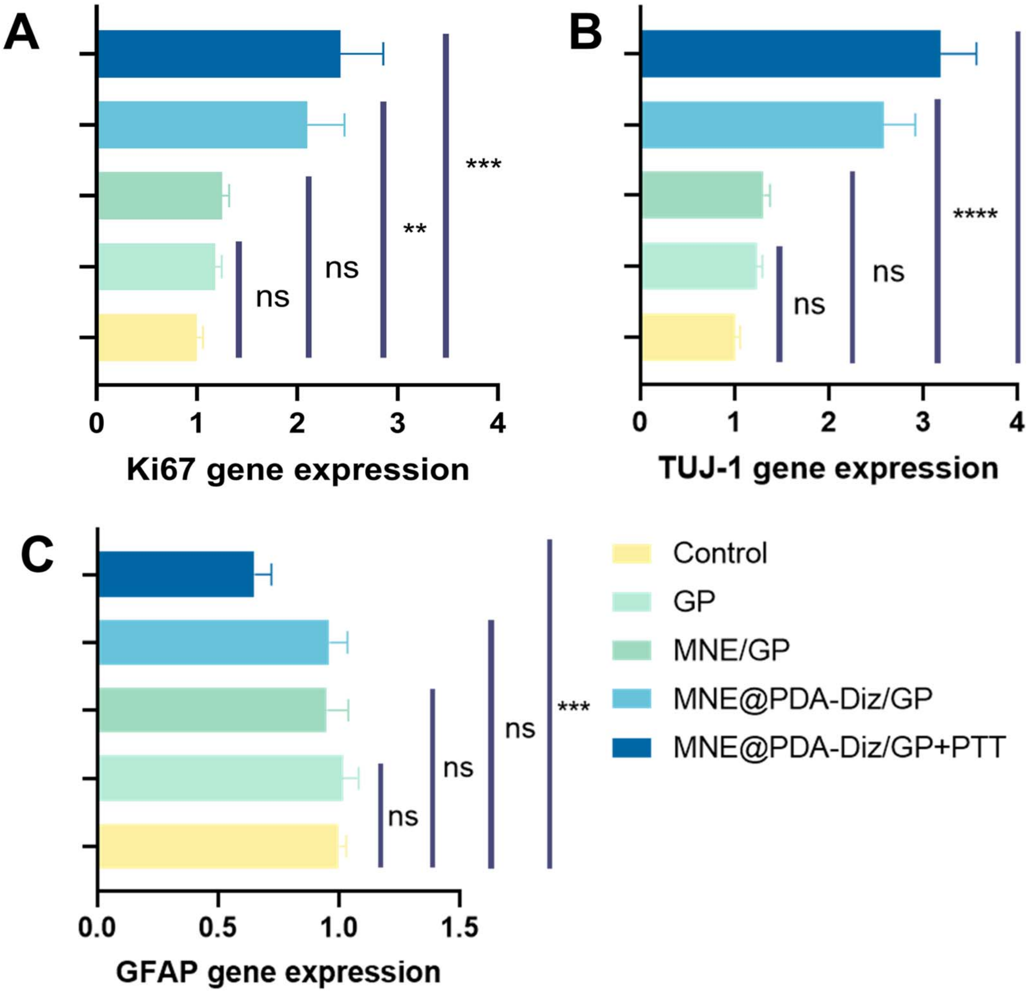

Fig. 20 The gene expression levels of Ki67 (A), TUJ-1 (B), and GFAP (C) in cells treated with GP, MNE/GP, MNE@PDA-Diz/GP, MNE@PDA-Diz/GP + PTT.

activation to block calcium overload and PDA-mediated PTT synergistically amplifies drug release and nanozyme activity. Collectively, the MNE@PDA-Diz/GP hydrogel effectively restores calcium homeostasis in neural cells, creating a favorable microenvironment for neuroprotection. The PTT-enhanced efficacy also validates the potential of spatiotemporally controlled photothermal-responsive hydrogels for precise spinal cord injury therapy.

Cell migration assays

Different materials were applied to the cells and tested the effects of the materials on cell migration. The results indicated that none of the materials exerted a significant impact on cell migration (Fig. 19). This may be because the 2-D culture did not provide sufficient structural support for the cells and lacked the microenvironment of 3-D culture. Due to the difficulty in detecting 3-D culture, the impact of materials on cell migration still needs to be explored.

Cell proliferation and differentiation assays

Ki67 expression levels were assessed to evaluate the effects of MNE@PDA-Diz/GP + PTT on cell proliferation (Fig. 20A). The Ki67 expression level was 1.00 ± 0.06 in the control group. The expression level of Ki67 in the GP group was 1.18 ± 0.07, while that in the MNE/GP group rose to 1.25 ± 0.07. In the MNE@PDA-Diz/GP group, the expression level was 2.10 ± 0.37. This enhancement occurs because of the proliferation-promoting effect of PDA. The expression level of Ki67 was observed to be the highest in MNE@PDA-Diz/GP + PTT group (2.43 ± 0.43), as PTT accelerated the release of PDA.

The effects of MNE@PDA-Diz/GP + PTT on differentiation ability of NSCs were detected by measuring gene expression levels of TUJ-1 (β-Tubulin III, the marker for neuronal cells) and GFAP (Glial Fibrillary Acidic Protein, the marker for astrocytes). TUJ-1 expression levels were analyzed to evaluate the effects of GP, MNE/GP, MNE@PDA-Diz/GP, and MNE@PDA-Diz/GP + PTT on presence of neuronal cells (Fig. 20B). The control group showed a TUJ-1 expression level of 1.01 ± 0.05 as the baseline. In the GP group, the expression level of TUJ-1 was 1.23 ± 0.06, while that in the MNE/GP group rose to 1.31 ± 0.07. The expression level in the MNE@PDA-Diz/GP group increased substantially to 2.58 ± 0.34, suggesting that PDA promoted the differentiation of neuronal cells. The expression level of TUJ-1 was observed to be the highest in the MNE@PDA-Diz/GP + PTT group (3.18 ± 0.38), as PTT enhanced the expression of heat shock proteins (HSPs). HSPs can regulate the remodeling process of thermosensitive matrices, stimulate the differentiation and maturation of neural stem cells, and promote dendrite outgrowth.[24] GFAP expression level was the inversion of TUJ-1 expression level. The GFAP expression levels were 1.00 ± 0.03, 1.02 ± 0.07, 0.95 ± 0.09 and 0.96 ± 0.08 in GP, MNE/GP, and MNE@PDA-Diz/GP groups, respectively. The MNE@PDA-Diz/GP + PTT group achieved the lowest level of GFAP expression of 0.65 ± 0.07, indicating reduced reactive gliosis and scar formation.[25]

Discussion

Developing effective SCI therapies remains a tough challenge, rooted in the intricate neural architecture of spinal cord, limited neuronal regenerative capacity, and the formation of an inhibitory injury microenvironment.[26] Conventional treatments, such as surgical decompression, corticosteroid administration, and rehabilitation, fall short of fully restoring neural function.[27] MNE@PDA-Diz/GP hydrogel addresses these challenges through a synergistic integration of components, leveraging their interconnected biological and physicochemical properties to modulate the injury microenvironment.

The efficacies of hydrogels stem from not only their individual actions but also the interplay between their components. MNE scavenges ROS to mitigate oxidative stress, which is a hallmark of secondary injury cascade of SCI.[23] PDA amplifies this effect *via* PTT. NIR-triggered PTT enhances ROS scavenging kinetics by accelerating nanozyme-ROS interactions and promoting controlled drug release,[28] which creates a spatiotemporally tuned antioxidant microenvironment, as seen in reduced calcium influx *via* FLUO-4 staining. Dizocilpine, an NMDAR antagonist, blocks excitotoxic calcium entry, with PDA catechol groups stabilizing dizocilpine within the hydrogel to ensure prolonged NMDAR blockade. This temporal coordination of MNE in early ROS clearance and dizocilpine sustained excitotoxicity inhibition aligns with pathophysiological timeline of SCI, where oxidative stress peaks acutely and excitotoxicity persists subacutely.

PDA acts as a biological orchestrator of the injury microenvironment. By polarizing macrophages to the anti-inflammatory M2 phenotype, it addresses SCI chronic inflammatory burden,[29] while its catechol-amine chemistry modulates NSC differentiation, favoring neuronal lineage commitment over astrogliosis. This dual action resolving inflammation and guiding regenerative differentiation targets two major repair barriers simultaneously. PDA first absorbs light to generate heat *via* its photothermal property. This elevated temperature then accelerates the release of MNE, dizocilpine and PDA, while also up-regulating neuronal HSPs.[24] The released PDA further enhances PTT efficiency, leading to increased local temperature.

Beyond providing basic structural support, the GP matrix orchestrates a multifaceted microenvironment by integrating specific mechanical and biochemical cues. First, the mechanical stiffness of the scaffold is recognized as a critical determinant of NSC fate. It is reported that NSCs preferentially differentiate into neurons on soft substrates (0.1–1 kPa), whereas stiffer matrices (7–10 kPa) promote glial lineage commitment.[30] The storage modulus of our MNE@PDA-Diz/GP hydrogel was formulated to be approximately 3.2 kPa, an intermediate stiffness leaning towards the softer, pro-neurogenic regime. This design actively fosters a mechanical microenvironment conducive to neuronal differentiation while potentially mitigating excessive astrogliosis.

Complementing this static mechanical guidance, the matrix provides dynamic, spatiotemporally controlled biochemical and physical signals. The RGD peptides of GelMA furnish crucial adhesive sites for NSC attachment and migration.[19] This adhesive landscape is dynamically modulated by the thermosensitive PNIPAM component. Upon reaching a temperature above 32 °C in PTT, PNIPAM undergoes a phase transition, causing localized shrinkage of the gel network.[21] This compaction serves a dual purpose: it concentrates the adhesive RGD ligands, potentially guiding and enhancing NSC migration, and simultaneously increases the local concentration of therapeutic agents (*e.g.*, dizocilpine) near the target site, enhancing local efficacy while minimizing systemic exposure.[31] Thus, the interplay between the tailored matrix stiffness, the biochemical adhesive motifs, and the thermally responsive structural dynamics creates a dynamically supportive, biomimetic niche that not only structurally bridges the injury but also actively instructs cellular behavior for neural repair.

While previous therapies struggle with survival and immune rejection[32] hydrogel synthesized in this work avoids these *via* material-mediated immunomodulation and localized delivery. However, translational challenges remain, because *in vitro* models simplify the 3-D complexity of the spinal cord. Future work must validate the hydrogel in SCI animal models, focusing on biomechanical integration, immunogenicity in long term, and scalability.

In summary, the MNE@PDA-Diz/GP hydrogel by coupling nanomaterial-enzyme interactions, photothermal responsiveness, and matrix mediated cell guidance, it succeeds in modulating calcium influx, ROS, inflammation, and cell differentiation, inspiring therapies for other CNS injuries or degenerative diseases with coexisting oxidative stress, inflammation, and regenerative failure.

Conclusions

In this study, a multifunctional thermosensitive hydrogel MNE@PDA-Diz/GP was developed to address multiple pathological challenges including oxidative stress and inflammatory responses during SCI repair. The hydrogel was fabricated by crosslinking GelMA and PNIPAM through photo-crosslinking technology to form a matrix network. Meanwhile, PDA-coated MNE loaded with dizocilpine was integrated into the hydrogel, constructing a composite system with both neuroprotective and neuroregenerative properties. This design fully integrates the cell-friendly matrix environment provided by GelMA, the temperature-responsive properties of PNIPAM, and the NIR-responsive PTT function mediated by PDA, thereby achieving precise spatiotemporal control over therapeutic effects. Experimental results showed that PTT could effectively accelerate the release of PDA and dizocilpine, significantly promoting the M2 macrophages polarization and inhibiting calcium influx. The synergistic effects of MNE and PDA endowed the hydrogel with strong ROS scavenging ability. The MNE@PDA-Diz/GP + PTT therapy improves cell proliferation activity and neuronal retention and reduces gliosis. In summary, this multitarget hydrogel can synergistically regulate key pathological processes including oxidative stress, inflammatory responses and neural regeneration, providing a potent and versatile therapeutic strategy for clinical repair of SCI.

Author contributions

Xing Gao: investigation, methodology, formal analysis, writing – original draft, writing – review & editing; Jingyan Sun: investigation, methodology, formal analysis, writing – original draft; Xin Bao:, investigation, methodology, formal analysis, validation; Mingsheng Xu: investigation, formal analysis, visualization; Chen Dong: funding acquisition, resources, supervision, writing – review & editing; Honghua Pan: methodology, funding acquisition, resources, supervision, writing – review & editing.

Conflicts of interest

There are no conflicts to declare.

Data availability

Most of the data supporting this article are available within the article. Due to confidentiality, any data not presented here can be made available subject to a non-disclosure agreement.

Acknowledgements

This work was financially supported by the Natural Science Foundation of Zhejiang Province (ZCLQ24C1002).

Notes and references

1 C. M. Mann and B. K. Kwon, *Semin. Spine Surg.*, 2007, **19**(4), 272–279.
2 F. Feng, X. Song, Z. Tan, Y. Tu, L. Xiao, P. Xie, Y. Ma, X. Sun, J. Ma, L. Rong and L. He, *Sci. Adv.*, 2023, **9**(25), eadg0234.
3 C. T. Trueblood, A. Singh, M. A. Cusimano and S. Hou, *Neuroscientist*, 2024, **30**(5), 597–611.
4 K. D. An, C. Y. Noh, J. Jang, W. T. Yuh and I. Choi, *Korean J. Neurotrauma*, 2025, **21**(4), 237–254.
5 Z. Lv, C. Dong, T. Zhang and S. Zhang, *Front. Bioeng. Biotechnol.*, 2022, **10**, 931800.
6 C. S. Ahuja, S. Nori, L. Tetreault, J. Wilson, B. Kwon, J. Harrop, D. Choi and M. G. Fehlings, *Neurosurgery*, 2017, **80**(3S), S9–S22.
7 K. Blot, J. Bai and S. Otani, *J. Physiol. Paris*, 2013, **107**(6), 448–451.
8 S. Hatfield, B. Belikoff, D. Lukashev, M. Sitkovsky and A. Ohta, *J. Leukoc. Biol.*, 2009, **86**(3), 545–548.
9 S. G. Carriedo, S. L. Sensi, H. Z. Yin and J. H. Weiss, *J. Neurosci.*, 2000, **20**(1), 240–250.
10 Y. J. Wei, H. Chen, Z. W. Zhou, C. X. Liu, C. X. Cai, J. Li, X. Q. Yu, J. Zhang, Y. H. Liu and N. Wang, *Small*, 2024, **20**(48), e2403679.
11 C. Jiang, J. Jia and S. Zhai, *Int. J. Mol. Sci.*, 2014, **15**(8), 13967–13992.
12 T. Clifford, Z. Finkel, B. Rodriguez, A. Joseph and L. Cai, *Cells*, 2023, **12**(6), 853.
13 X. He, E. Obeng, X. Sun, N. Kwon, J. Shen and J. Yoon, *Mater. Today Bio*, 2022, **15**, 100329.

14 B. Zhang, Q. Li, Q. Xu, B. Li, H. Dong and Y. Mou, *Int. J. Nanomed.*, 2023, **18**, 4601–4616.

15 W. Pi, Y. Zhang, L. Li, C. Li, M. Zhang, W. Zhang, Q. Cai and P. Zhang, *Biofabrication*, 2022, **14**(3), 035006.

16 C. Li, S. Y. Liu, M. Zhang, W. Pi, B. Wang, Q. C. Li, C. F. Lu and P. X. Zhang, *Neural Regen. Res.*, 2022, **17**(9), 2050–2057.

17 Z. Tong, L. Jin, J. M. Oliveira, R. L. Reis, Q. Zhong, Z. Mao and C. Gao, *Bioact. Mater.*, 2020, **6**(5), 1375–1387.

18 L. P. da Silva, M. T. Cerqueira, R. A. Sousa, R. L. Reis, V. M. Correlo and A. P. Marques, *Acta Biomater.*, 2014, **10**(11), 4787–4797.

19 M. Sun, X. Sun, Z. Wang, S. Guo, G. Yu and H. Yang, *Polymers*, 2018, **10**(11), 1290.

20 S. Gupta, A. Singh and N. Matsumi, *ACS Omega*, 2019, **4**(25), 20923–20930.

21 R. D. Bartlett, D. Eleftheriadou, R. Evans, D. Choi and J. B. Phillips, *Biomaterials*, 2020, **258**, 120303.

22 J. Wang, Y. Wang, X. Xiaohalati, Q. Su, J. Liu, B. Cai, W. Yang, Z. Wang and L. Wang, *Adv. Sci.*, 2023, **10**(20), e2206854.

23 J. Zhang, Z. Wang, X. Lin, X. Gao, Q. Wang, R. Huang, Y. Ruan, H. Xu, L. Tian, C. Ling, R. Shi, S. Xu, K. Chen and Y. Wu, *Angew Chem. Int. Ed. Engl.*, 2025, **64**(4), e202416686.

24 S. Jung, N. Harris, II. Niyonshuti, S. V. Jenkins, A. M. Hayar, F. Watanabe, A. Jamshidi-Parsian, J. Chen and M. J. Borrelli, *Nanomaterials*, 2021, **11**(5), 1216.

25 M. Darvishi, T. Tiraihi, S. A. Mesbah-Namin, A. Delshad and T. Taheri, *Neurochem. Res.*, 2014, **39**(12), 2319–2333.

26 H. Suzuki and T. Sakai, *Int. J. Mol. Sci.*, 2021, **22**(14), 7435.

27 D. C. Baptiste and M. G. Fehlings, *Prog. Brain Res.*, 2007, **161**, 217–233.

28 Z. Yuan, J. Wu, Y. Xiao, H. Yang, S. Meng, L. Dai, P. Li and K. Cai, *Adv. Funct. Mater.*, 2023, **33**(37), 2302908.

29 S. Xia, D. Liu, K. Jiang, M. Cao, Z. Lou, R. Cheng, J. Yi, A. Yin, Y. Jiang, K. Cheng, W. Weng, B. Shi and B. Tang, *Mater. Today Bio*, 2024, **27**, 101156.

30 M. Shu, X. Xue, H. Nie, X. Wu, M. Sun, L. Qiao, X. Li, B. Xu, Z. Xiao, Y. Zhao, Y. Fan, B. Chen, J. Zhang, Y. Shi, Y. Yang, F. Lu and J. Dai, *Sci. China Life Sci.*, 2022, **65**(2), 295–308.

31 Y. S. Kim, M. A. Kim and C. M. Lee, *Mater. Technol.*, 2019, **34**(11), 639–644.

32 L. Wertheim, R. Edri, Y. Goldshmit, T. Kagan, N. Noor, A. Ruban, A. Shapira, I. Gat-Viks, Y. Assaf and T. Dvir, *Adv. Sci.*, 2022, **9**(11), e2105694.